Sustainable Marine Structures
https://journals.nasspublishing.com/index.php/sms

ARTICLE

High-Precision Offshore Wind Energy Assessment Using SAR Satellite Data: A Case Study of Zhuanghe Offshore Waters

Ling Yuan* , ***Haichuan Long*** , ***Xia Ruan, Fengzhi Yang, Jianke Li, Peng Chen***

China State Shipbuilding Corporation (CSSC) Haizhuang Windpower Co., Ltd., Chongqing 401123, China

ABSTRACT

With growing global demand for clean energy, offshore wind resource assessment is crucial. This study comprehensively utilizes multi-source Synthetic Aperture Radar (SAR) satellite data, including European Sentinel-1 and Chinese Gaofen-3 satellites, along with in-situ wind mast measurements, to systematically assess the wind energy resources in the offshore area of Zhuanghe, Liaoning Province, China, from 2017 to 2022. Sea surface wind fields were retrieved through data preprocessing, polarization conversion, geophysical model inversion, and multi-source data fusion. By coupling a vertical extrapolation model that accounts for sea state effects, the 10-m wind speeds were extrapolated to turbine hub heights of 40 m, 80 m, and 100 m, enabling the calculation of key wind energy parameters such as wind speed and wind power density. Results indicate that at 100 m height, the annual average wind speed is 6.40 $m \cdot s^{-1}$ and the annual average wind power density is 312.8 $W \cdot m^{-2}$, corresponding to wind class 2. Wind speeds are higher in spring and winter and lower in summer and autumn, with prevailing northerly winds. Compared with ERA5 reanalysis data, SAR data offer advantages including high spatial resolution, rich historical records, and superior local accuracy, making them suitable for detailed offshore wind resource assessment. This research fills the gap in high-precision wind energy evaluation under complex meteorological and data-scarce con-

*CORRESPONDING AUTHOR:
Ling Yuan, China State Shipbuilding Corporation (CSSC) Haizhuang Windpower Co., Ltd., Chongqing 401123, China; Email: 18614047730@163.com

ARTICLE INFO
Received: 17 December 2025 | Revised: 22 January 2026 | Accepted: 3 February 2026 | Published Online: 25 February 2026
DOI: https://doi.org/10.36956/sms.v8i1.3004

CITATION
Yuan, L., Long, H., Ruan, X., et al., 2026. High-Precision Offshore Wind Energy Assessment Using SAR Satellite Data: A Case Study of Zhuanghe Offshore Waters. Sustainable Marine Structures. 8(1): 142–166. DOI: https://doi.org/10.36956/sms.v8i1.3004

ditions in the region, provides reliable data support for local offshore wind farm planning and development, and offers transferable experience for the application of SAR technology in similar coastal areas in China.

Keywords: Synthetic Aperture Radar (SAR); Wind Resource Assessment; Offshore; Zhuanghe Wind Farm; Vertical Extrapolation; Wind Energy Potential

1. Introduction

In recent years, the global demand for clean and renewable energy has been on a continuous upward trajectory, driving a rapid acceleration in wind energy development. Among various wind energy forms, offshore wind energy has attracted extensive attention as it offers distinct advantages, such as higher wind speed, more stable wind resources and reduced land use conflicts [1, 2]. However, accurate assessment of wind resources is crucial for the successful planning, design and operation of wind energy projects. Synthetic Aperture Radar (SAR) satellites have become a potent tool for wind resource assessment, particularly in offshore regions where in-situ measurements are scarce and challenging to obtain [3, 4]. SAR sensors can capture high-resolution images of the Earth's surface, enabling the retrieval of wind fields over vast oceanic areas with a spatial resolution of approximately 200 m [5].

One of the widely adopted methods for retrieving wind speed from SAR images is based on the Geophysical Model Functions (GMFs). The GMFs establish a quantitative relationship between the radar backscatter measured by SAR sensors and sea-surface wind speed and direction [6]. The first-generation GMFs, such as the CMOD4 and the CMOD5, which were initially developed for scatter-meter data, have been successfully used for SAR data [7, 8]. Both CMOD4 and CMOD5.N are C-band Geophysical Model Functions (GMFs) developed by the Royal Netherlands Meteorological Institute (KNMI). They are used to establish the empirical relationship between the backscatter coefficients measured by spaceborne scatter-meters and the sea surface 10 m wind vectors. CMOD4, developed based on ERS-1 data, is suitable for wind speeds ranging from 0 to 24 $m \cdot s^{-1}$ and supports wind retrieval for early ERS series satellites; CMOD5.N, as its upgraded version, features optimized neutral wind output and improved accuracy in high wind speed ranges, is compatible with the ASCAT scatterometer, can retrieve wind speeds from 0 to 30 $m \cdot s^{-1}$, and is widely applied in operational wind field retrieval, extreme wind condition monitoring, and offshore wind energy assessment. These early GMFs generally assume a neutral atmospheric boundary layer and a fully developed sea state. Subsequent improvements, such as the CMOD5.N for near-shore areas and non-neutral stratification [9] and the VV-polarization GMF for Sentinel-1 SAR data under high-wind conditions [10], aim to account for more complex scenarios. Accurate wind direction information is vital for wind velocity retrieval using the GMFs. Wind direction data can be sourced from numerical weather prediction (NWP) models, buoy measurements and SAR images. Analyzing wind streaks and Bragg waves in SAR images is a common method for wind direction retrieval [11]. Additionally, polarimetric SAR data can provide more detailed information about the polarization state of radar backscatter to infer wind direction [12], although it requires more advanced processing algorithms compared with single-polarization data. Machine learning techniques have gained increasing popularity in SAR wind retrieval. Algorithms such as artificial neural networks and support vector machines can learn the complex relationship between SAR backscatter and wind speed or direction without relying on explicit physical assumptions [13–15]. These approaches have shown great potential in improving retrieval accuracy, especially in complex coastal and nearshore regions. However, they demand a large amount of training data, are computationally intensive and often suffer from interpretability issues.

Several SAR satellites serve as important data sources for wind resource assessment. The data from the Sentinel-1 mission, which was launched by the European Space Agency (ESA) in 2014, are widely used. Comprising Sentinel-1A and Sentinel-1B, the Sentinel-1 mission operates in a sun-synchronous polar orbit, providing data with global coverage at high temporal resolutions (6 days or 3 days for dual satellite operation) and spatial resolution (5 m in Strip-map mode and 20 m in Interferometric Wide Swath mode) [16]. Its

freely available data through the Copernicus Open Access Hub has been utilized in numerous offshore wind resource studies [17, 18]. RADARSAT-2, a Canadian SAR satellite launched in 2007, offers various imaging modes with different resolutions, swath widths and polarization options. RADARSAT-2 SAR data have been used for wind resource assessment in regions such as the Canadian Arctic and coastal areas [19, 20], and its multi-polarization capabilities are useful in complex environments. The Advanced Land Observing Satellite-2 and Daichi-2, launched by the Japan Aerospace Exploration Agency in 2014, carry Phased Array type L-band Synthetic Aperture Radar (PALSAR-2) sensors with a high spatial resolution of up to 3 m. Although mainly designed for terrestrial observations, their data have also been applied to wind resource assessment in coastal and off-shore regions [21], and the L-band frequency of the PALSAR-2 sensor provides better cloud and vegetation penetration. Other SAR satellites, such as the Chinese Gaofen-3 (GF-3) satellite [22, 23] and the Indian RISAT-1 and RISAT-2 satellites [24], have also made contributions to wind resource assessment in specific areas or on a limited scale.

Validating SAR wind retrievals is of critical importance. In-situ measurements from buoys, masts and ships are commonly used as reference data. Statistical metrics, including root-mean-square error (RMSE), mean absolute error (MBE), mean bias (MB) and correlation coefficient (R), are employed to evaluate the accuracy of SAR wind retrievals. In open ocean areas, SAR wind retrievals typically exhibit an RMSE of about 1–2 m s^{-1} and a bias of less than ±1 m s^{-1}. However, in coastal regions, the accuracy may decrease due to various complex factors [25–28]. Comparing SAR wind retrievals with NWP model outputs is another common validation approach. While NWP models can simulate atmospheric states and wind fields, they also have inherent uncertainties. In some cases, SAR retrievals can offer more accurate local wind pattern information, especially in areas where NWP models struggle to resolve small-scale features [29, 30]. Inter-comparing different SAR products from the same or different satellites with each other can help identify the strengths and weaknesses of algorithms and data sources. Such comparisons have demonstrated good agreement in open ocean areas but revealed differences in coastal regions and under certain weather conditions [31–34].

The SAR has been widely applied in wind resource assessment due to its ability to provide high-resolution, spatially continuous observations of near surface wind fields over ocean surfaces [35–38]. In offshore wind farm planning, SAR data support the identification of suitable locations by characterizing wind resource availability, temporal variability, and environmental constraints. Additionally, SAR data aid in optimizing wind turbine layout to maximize energy yield and mitigate wake losses [39–42]. For wind resource monitoring and forecasting, the SAR enables continuous monitoring of wind resources in offshore areas, which is beneficial for operational optimization, maintenance scheduling, and power output management. Furthermore, SAR data can also be assimilated into NWP models to enhance the accuracy of wind forecasts [38, 43–45]. In remote or data sparse areas, such as the Arctic region and open oceans where in-situ conventional measurements are scarce, the SAR serves as a valuable tool for evaluating wind resource potential, especially over large ice covered and open water surfaces [46–48].

Despite significant advancements in SAR wind field retrieval technology worldwide, the application of its retrieval results in engineering practice remains relatively limited in China. As a key area for offshore wind power planning in northern China, the offshore waters near Zhuanghe City, Liaoning Province, are a typical data scarce region: restricted by terrain and located 10–50 km offshore, coastal conventional meteorological stations fail to provide sufficient coverage, while offshore buoy observations suffer from short monitoring periods and poor data continuity. Additionally, mesoscale reanalysis data such as ERA5 cannot capture local wind field distortions due to insufficient resolution, making it difficult to meet engineering accuracy requirements. Furthermore, this area features unique marine meteorological conditions characterized by the superposition of a temperate monsoon climate and the Yellow Sea environment, the confluence of the Yellow Sea Warm Current and coastal cold water masses, and fragmented terrain, resulting in a complex wind field pattern. Cur-

rently, there is a severe lack of research on SAR wind field retrieval and verification for such scenarios, combining "data scarcity and complex meteorological conditions" in this region, as well as a shortage of suitable high-precision wind resource assessment results to support local offshore wind power development. Based on this, relying on the latest achievements in SAR-based wind resource assessment, this study focuses on a detailed case analysis of the offshore waters near Zhuanghe. It not only fills the scientific gaps and engineering data bottlenecks in high-precision wind resource assessment under complex environments in this region, providing reliable support for local wind farm site selection and power generation calculation, but also offers replicable experience for the application of SAR technology in similar offshore areas in northern China, promoting the widespread implementation of SAR data in wind resource assessment.

2. Materials and Methods

2.1. Study Area

The research region in this study is in the offshore area of Zhuanghe City, administered by Liaoning Province, China (**Figure 1**). Geographically, it lies on the southern coast of the eastern Liaodong Peninsula, along the northern margin of the Yellow Sea. This region falls within the northern temperate zone and is characterized by a warm temperate humid continental monsoon climate with distinct maritime influences. The climate features mild conditions with four distinct seasons, a strong concurrence of heat and precipitation during summer, concentrated rainfall events, ample sunshine, and prevailing monsoonal wind. The average diurnal temperature range remains below 10 °C throughout the year. The Zhuanghe offshore area is a shallow inland sea, with marked seasonal variations in sea surface temperature. In summer, the average surface water temperature is approximately 26.3 °C, while in winter, it can drop to as low as −2.7 °C. The main types of submarine landforms are shallow marine zones and shallow sea accumulation plains. The area within the 0–10 m isobaths is 10 km wide, featuring a flat and homogeneous seabed. Beyond this depth, the seafloor is composed primarily of underwater accumulation plains with smooth topography, providing highly favorable conditions for the construction of offshore wind farms.

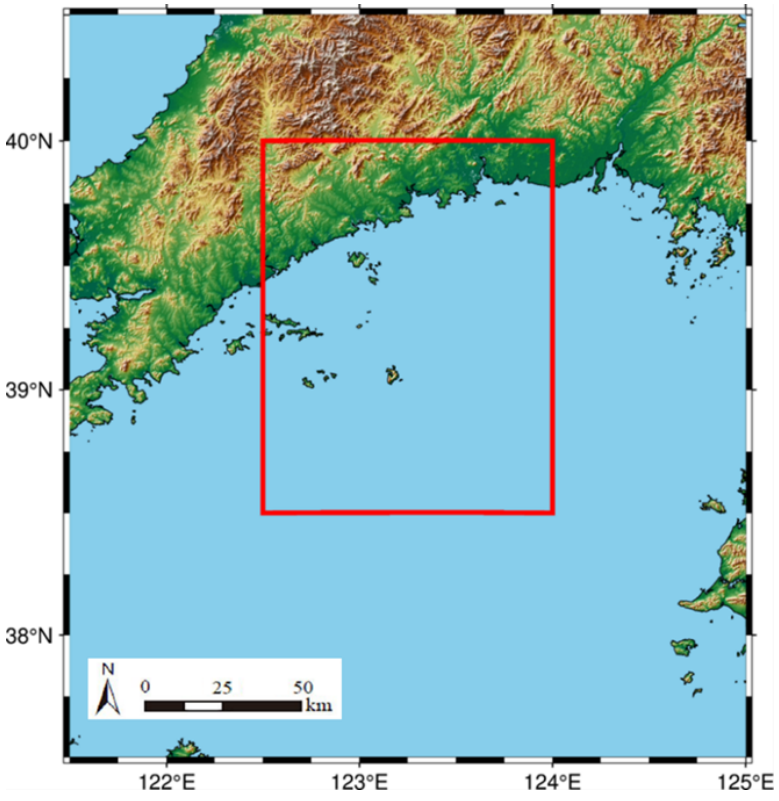

Figure 1. Map of the study area.

2.2. Data Collection and Processing

2.2.1. Multi-Source SAR Satellite Data

This study primarily utilizes the datasets acquired from the Sentinel-1 SAR satellite, Gaofen-3 (GF-3) satellite, and the C-band Synthetic Aperture Radar (SAR) satellite series for analysis.

(1) **Gaofen-3 Satellite**

The GF-3 satellite is the first high-resolution C-band SAR satellite developed for civilian applications in China's High-resolution Earth Observation System major project. It is capable of acquiring SAR imagery with a spatial resolution of 1 m, features high resolution and supports multiple polarization modes, a wide range of imaging configurations and extended operational duration. The GF-3 SAR payload exhibits advanced features including multi-polarization imaging, large-aperture antenna design, high power and radiometric resolution better than 2 dB. Its continuous imaging capability of up to 50 min and integrated internal/external calibration functions enhance its utility for quantitative applications. The satellite provides C-band SAR imagery with spatial resolutions ranging from 1 m to 500 m and swath widths between 10 km and 650 km. Under optimal conditions, its radiometric accuracy can reach up to 1 dB.

(2) **C-SAR Satellite**

The C-SAR satellites (C-SAR-01 and C-SAR-02) are two operational follow-on satellites to the GF-3 satellite and represent the first Chinese operational SAR satellites in orbit. These satellites carry advanced C-band multi-polarization SAR payloads and incorporate several performance enhancements, including an integrated Automatic Identification System signal reception system, improved spatial resolution and observation swath width in the wave mode, enhanced capabilities for ocean wave monitoring, extended daily observation duration, and improved operational efficiency and availability.

The satellites support global observation coverage, with real-time imaging spanning latitudes 5°S to 50°N and longitudes 70°E to 150°E. In single-satellite operation, the aver-age revisit cycle is less than 3 days in the single side-looking mode. Under the dual-side-looking mode at a 10 m resolution and a 100 km imaging swath, 90% of the real-time observation area has a revisit cycle of less than 1.5 days. When operating as a three satellite constellation, the average revisit cycle is reduced to less than 1 day in the single-side-looking mode, and 90% of the coverage area has a revisit cycle of less than 18 h in the dual-side-looking mode at a 10 m resolution and a 100 km swath. The constellation operates in a nominal 29-day repeat orbit (418 orbital tracks), ensuring systematic and reliable Earth observations.

(3) **Sentinel-1 Satellite**

The Sentinel-1 satellite series, the successors to the ERS-1/2 and EnviSat missions, form a critical component of the ESA's Copernicus Program for global environmental and security monitoring. The constellation is planned to consist of four near-polar sun-synchronous satellites: Sentinel-1A, Sentinel-1B, Sentinel-1C and Sentinel-1D. Sentinel-1A and Sentinel-1B satellites were successfully launched on April 3, 2014 and April 25, 2016, respectively. The sentinel-1C satellite was scheduled for launch in the first half of 2023, while the Sentinel-1D satellite is not yet on the launch schedule. Each satellite is equipped with a C-band SAR operating at a frequency of 5.405 GHz and follows a near-polar sun-synchronous orbit with a 12-day repeat cycle. The orbital period is 98.74 min. The ascending pass (crossing the northbound equator) occurs at approximately 18:00 local time, while the descending pass (crossing the southbound equator) occurs at around 06:00 local time.

(4) **Collection and Statistics of Satellite Data**

In this research, a total of 600 samples of SAR images of the target area in the Zhuanghe offshore waters are obtained (**Table 1**). Specifically, there are 157 samples in 2017, 174 samples in 2018, 245 samples in 2019, 132 samples in 2020, 205 samples in 2021 and 50 samples in 2022.

2.2.2. Retrievals of Sea Surface Wind Fields from SAR Data

The retrieval of sea surface wind fields based on SAR data is a method that employs microwave remote sensing technology to obtain high-resolution information on sea surface wind speed and wind direction. The core processes of this method include data preprocessing, polarization transformation, the application of geophysical models, wind direction deblurring and accuracy verification (**Figure 2**). The specific steps are as follows.

Table 1. Distribution of the years and months of the images used for the assessment of offshore wind energy resources in Zhuanghe.

Years	Sample Size	Monthly Sample Size											
		Jan	Feb	Mar	Apr	May	Jun	Jul	Aug	Sept	Oct	Nov	Dec
2017	157	8	7	14	15	14	15	13	15	15	17	13	11
2018	174	15	14	12	17	13	15	12	16	15	15	15	15
2019	245	21	14	25	20	27	21	24	21	16	19	16	21
2020	232	15	18	20	18	19	20	22	20	21	22	18	19
2021	205	14	13	15	15	9	17	24	20	19	21	20	18
2022	50	5	5	5	5	5	4	2	3	4	6	5	1
Total	1063	78	71	91	90	87	92	97	95	90	100	87	85

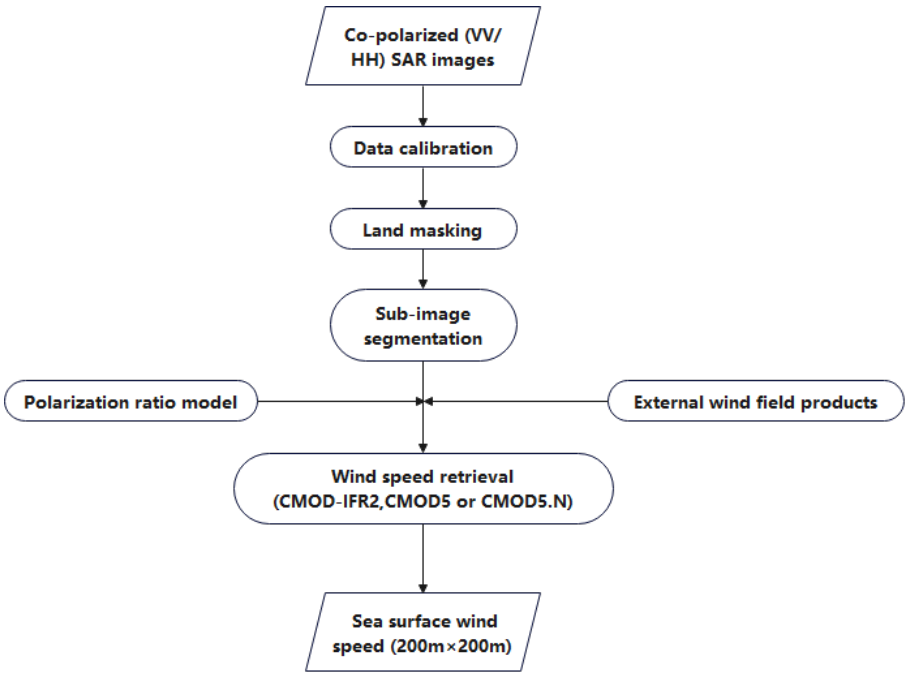

Figure 2. Flow chart of the retrieval of Synthetic Aperture Radar (SAR) sea surface wind.

(1) **Data Preprocessing**

◆ **Radiometric Calibration**

Convert the gray values (DN) of the raw SAR images to normalized radar backscatter coefficients (σ^0). For different satellites (such as GF-3 and Sentinel-1), specific calibration formulas are used. For example, the formula [49] for the GF-3 satellite is:

$$\sigma^0 = \mathrm{DN}^2 \left(\frac{M}{65535} \right)^2 - N[dB] \quad (1)$$

where M denotes the external calibration factor, and N is a constant.

◆ **Land Masking**

Use the ETOPO1 topographic data to generate a binary land-sea mask, eliminate land areas, and retain only ocean pixels.

◆ **Noise Reduction Processing**

Employ the enhanced Lee filtering algorithm to suppress speckle noise. Divide the image into uniform regions, weak texture regions and non-uniform regions according to the local standard deviation coefficients, and separately perform mean filtering or retain the original values.

◆ **Bright Target Removal**

Detect bright targets such as ships through the Constant False Alarm Rate algorithm. Set the background window and protection window, calculate detec-

tion thresholds using the Gaussian distribution model, and mark and remove abnormal pixels.

(2) Polarization Conversion

For HH-polarized SAR data, it is necessary to convert it into equivalent VV-polarized data through a polarization ratio model (such as the Elfouhaily model), as shown in Equation (2).

$$PR_{Elfouhaily} = \frac{\left(1 + 2\tan^2\theta\right)^2}{\left(1 + 2\sin^2\theta\right)^2} \tag{2}$$

where θ represents the radar incident angle. The polarization ratio model ensures the applicability of the CMOD series models, which are only applicable to VV polarization.

(3) Retrieval Through Geophysical Model Functions

Use the semi-empirical model CMOD5.N to relate σ^0, θ, relative wind direction (φ) and wind speed (u_{10}), as shown in Equation (3).

$$\begin{aligned}\sigma_{\mathrm{VV}}^0 = B_0\left(\theta, u_{10}\right)\left[1+ \quad B_1\left(\theta, u_{10}\right)\cos\varphi + \right. \\ \left. B_2\left(\theta, u_{10}\right)\cos 2\varphi\right]^n\end{aligned} \tag{3}$$

where B_0, B_1, and B_2 indicate the coefficients related to the wind speed and the incident angle, and φ denotes the angle between the wind direction and the radar sight line. The model is adjusted and optimized with 28 coefficients and is suitable for the retrieval of medium and high wind speed.

(4) Wind Direction Deblurring

◆ **Wind Stripe Analysis**

In terms of SAR images with wind stripes (formed by the periodic variations of sea surface roughness), the Local Gradient method is used to extract the initial wind direction, in order to solve the 180° ambiguity problem.

◆ **External Data Assistance**

If wind stripes are not available, wind direction information is obtained by interpolating scatterometry data (e.g., Advanced scatterometry data) or numerical simulations (such as the ERA5 product).

(5) Multi-Source Data Fusion

Combine the multi-source SAR satellite data (2017–2022) from the Sentinel-1, GF-3, C-SAR and other satellites, which cover different temporal and spatial resolutions, to enhance the continuity and regional representativeness of wind field series. For instance, the Interferometric Wide Swath mode of the Sentinel-1 satellite provides data with a swath width of 250 km, and the GF-3 satellite supports observations with resolutions ranging from 1 m to 500 m.

2.2.3. Sea Surface Wind Speed Vertical Extrapolation Method

The purpose of this subsection is to address the issue that the sea state effect is not considered in the current sea surface wind speed vertical extrapolation technology. With reference to the research findings of Nie and Li[50], a statistical model-based parameterization method for the sea surface roughness length is proposed and coupled with the logarithmic wind profile scheme, so as to achieve high-precision vertical extrapolation of wind speed at the reference height. The steps of this method are as follows:

Step 1: The random wind speed sequence $v_0$at a single site at the reference height can be regarded as v_0 = V_{ave} + ΔV. Among them, the V_{ave} is almost stable during the service life of wind turbines, and the ΔV can be regarded as a random sequence reflecting the effects of short-term weather patterns and turbulent fluctuations.

Step 2: The marine atmospheric boundary layer exerts a profound influence on the wind speed profile mainly through its thermal stratification state and sea state. The stability of the atmospheric boundary layer can be divided into seven categories: very stable, stable, near-neutral/stable, neutral, near-neutral/unstable, unstable, and very unstable. For most of the time, the marine atmospheric boundary layer is in a neutral or near-neutral stratification state. Therefore, under the assumption of neutral stratification, the logarithmic wind speed profile can be used to extrapolate the wind speed at height z from v_0, as shown below:

$$\frac{v(z)}{v_0} = \frac{ln(z) - ln\left(z_0\right)}{ln10 - ln\left(z_0\right)} \tag{4}$$

The sea surface roughness length $z_0$can be expressed as $z_0 = z_{0*}u_*^2/g$, where g is the gravitational acceleration, friction velocity $u_*$is the friction velocity, and α is the Charnock parameter, which takes a value

of 0.011 for open ocean areas. The u_* depends on the wind speed v_0 and the drag coefficient C_d. Previous studies have shown that the sea surface roughness length is mainly related to wind speed and wave age, and z_0 can usually be written as $z_0 = z_{0*} f\left(C_d,\ u_*, v_0\right)/g$.

Step 3: Since it is still difficult to obtain the real-time distribution of sea wave age at the regional scale at present, a practical approach is to parameterize the statistical relationship ($u_*^2 = f_*\left(v_0\right)$) between u_*^2 and $v_0$based on in-situ observations, in which the effect of sea wave age is considered statistically. Then, the wind speed adjustment factor in Equation (4) can be decomposed into

$$\frac{v(z)}{v_0} = 1 + \zeta\left(z, V_{ave}\right) + ln\left(\frac{z}{10}\right)\Phi\left(\Delta V, V_{ave}\right) \quad (5)$$

$$\zeta\left(z, V_{ave}\right) = \frac{ln(z) - ln(10)}{ln(10) - ln\left(z_{0*} f_*(V_{ave})/g\right)} \quad (6)$$

$$\Phi\left(\Delta V, V_{ave}\right) = \frac{ln\left(f_*(V_{ave} + \Delta V)\right) - ln(f_*(V_{ave}))}{\left[ln(10) - ln(z_{0*} f_*(V_{ave} + \Delta V)/g)\right]\left[ln(10) - ln(z_{0*} f_*(V_{ave})/g)\right]} \quad (7)$$

where $\zeta(z,\ V_{ave})$ reflects the effect of the long-term mean wind speed, and $\Phi(\Delta V, V_{ave})$ reflects the effect of the short-term wind speed deviation.

Step 4: To determine $\zeta(z,\ V_{ave})$ and $\Phi(\Delta V, V_{ave})$, based on the expression of u_*^2, this is converted to determining the statistical relationship between the drag coefficient C_d and v_0. Based on the experimental results, $f_*(v_0)$ can be expressed as $f_*\left(v_0\right) = Av_0^4 + Bv_0^3 + Cv_0^2 + Dv_0 + E$. The unknown coefficients A, B, C, D and E are determined via polynomial fitting, with their specific values as follows: A = −4.347 × 10^{-6}, B = 2.732 × 10^{-4}, C = −2.760 × 10^{-3}, D = 2.042 × 10^{-2}, E = −0.03576. Therefore, $\zeta(z,\ V_{ave})$ can be derived using Equation (6).

Step 5: $\Phi(\Delta V, V_{ave})$ is further subjected to rational simplification using $f_*(v_0)$ equation. Experimental results show that for common long-term mean offshore wind speeds (ranging from 5 to 8 m/s), $\Phi(\Delta V, V_{ave})$ is actually insensitive to V_ave and $\Phi(0,\ V_{ave})$is equal to zero. Therefore, $\Phi(\Delta V, V_{ave})$ can be reasonably approximated as a linear function of $k\Delta V$, where k is a constant. In this study, the constant coefficient k is taken as 0.0019 $(\mathrm{m/s})^{-1}$, which is obtained via linear fitting. The deviation of $f_*(v_0)$ caused by this simplification is usually less than 0.005, and the simplification of $f_*(v_0)$ will introduce a maximum deviation of 1% at most to the wind speed at the wind turbine hub height (e.g., 100 m). That is to say, the deviation of the wind power density (WPD) at a single site caused by the simplification of $f_*(v_0)$ is at most about 3%.

Step 6: By substituting Equation $\Phi(\Delta V, V_{ave})$ into Equation (5), we obtain the wind speed at height z, namely:

$$\frac{v(z)}{v_0} = 1 + \zeta\left(z, V_{ave}\right) + kln\left(\frac{z}{10}\right)\Delta V \quad (8)$$

2.2.4. Probability Distribution Model of Wind Speed

Typically, wind velocity in nature has relatively large fluctuations. In order to grasp the average situation of wind velocity as comprehensively as possible, a large number of measurements is often required for analysis, and it is particularly cumbersome to do statistics and collation of observations. Therefore, some scholars have proposed using probability density functions to describe wind speed frequency distributions. These probability density functions include the Rayleigh distribution, the three-parameter Weibull distribution and the two-parameter Weibull distribution. Numerous studies have shown that the two-parameter Weibull distribution function is more suitable for describing wind speed frequency distributions, and its mathematical expression can be written as:

$$f(v) = \frac{k}{c}\left(\frac{v}{c}\right)^{k-1}\exp\left[-\left(\frac{v}{c}\right)^k\right](v > 0) \quad (9)$$

where $f(v)$ represents the occurrence probability of wind speed v, and c and k denote the scale and shape parameters of the Weibull distribution, respectively. The probability distribution of wind speed is shown in **Figure 3**.

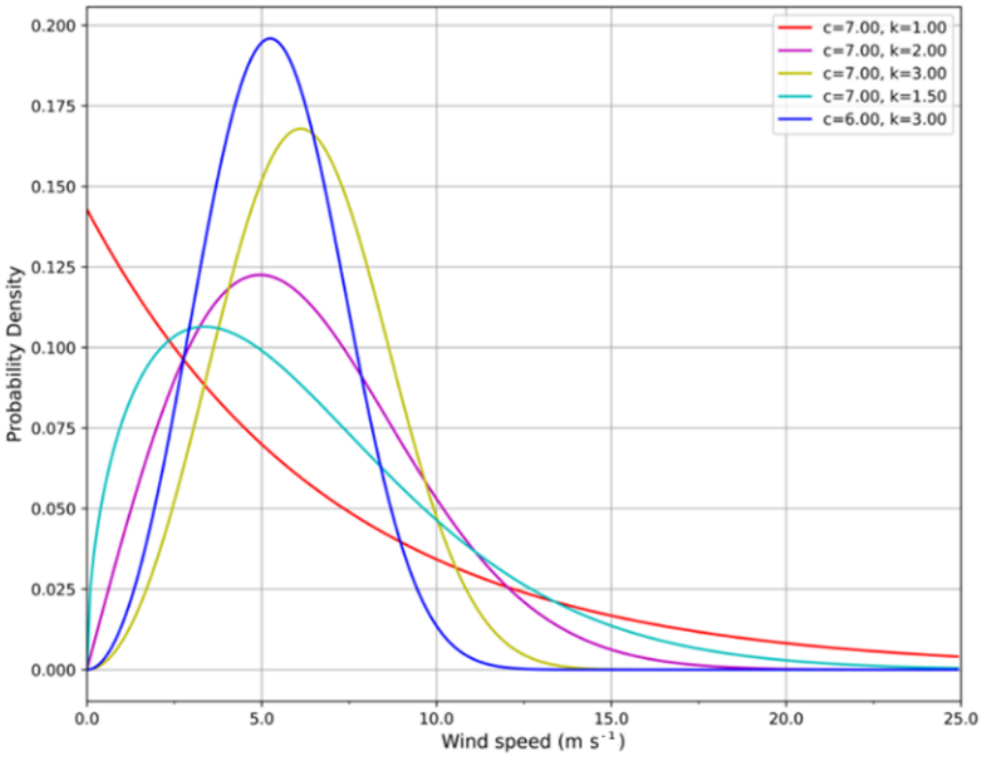

Figure 3. Weibull probability density curve.

2.2.5. In-Situ Measurements

In this study, the measurements from three wind measurement towers in the study area are collected to validate the findings of wind resource data. Limited by the temporal mismatch between the in-situ measurement data and the partial time series of SAR in this study, we conducted representative year correction for the two datasets separately before performing comparative verification. The specific information on the wind measurement towers is shown in **Table 2**:

Table 2. Basic information on the three wind measurement towers.

Sites	Longitude/Latitude	Height	Observation Period
Mast 4#	123.320°E/39.593°N	10 m, 40 m, 60 m, 70 m, 80 m, 90 m	2015.11.16–2017.11.13
Mast 5#	123.203°E/39.509°N	10 m, 40 m, 60 m, 70 m, 80 m, 90 m	2015.11.16–2017.11.16
Mast 6#	123.297°E/39.399°N	10 m, 40 m, 60 m, 70 m, 80 m, 90 m	2015.11.16–2017.11.16

2.3. Assessment Metrics

Three assessment metrics are used to evaluate the SAR-derived retrievals (M_i) based on meteorological mast measurements (G_i): (1) correlation coefficient (R), which is used to assess the quality of data fitting; (2) mean bias (MB), which may be positive (overestimation) or negative (underestimation) and is used to for comparison between SAR-derived retrievals and site measurements; (3) root mean square error ($RMSE$), which measures the change in the calculated values relative to site measurements. The three indicators can be calculated through Equations (10)–(12):

$$R = \frac{\sum_{i=1}^{n}\left(G_i - \overline{G}\right)\left(M_i - \overline{M}\right)}{\sqrt{\sum_{i=1}^{n}\left(G_i - G\right)^2}\sqrt{\sum_{i=1}^{n}\left(M_i - \overline{M}\right)^2}} \tag{10}$$

$$RMSE = \sqrt{\frac{1}{N}\sum_{i=1}^{n}\left(G_i - M_i\right)^2} \tag{11}$$

$$MB = \frac{1}{N}\sum_{i=1}^{n}\left(M_i - G_i\right) \tag{12}$$

where M_i and G_i denote the SAR-derived retrievals and in-situ observations, respectively, and $\overline{M}$ and $\overline{G}$ represent their respective means.

3. Results

3.1. Meteorological Conditions

3.1.1. Analysis of Wind Measurement Tower Data

Understanding the meteorological background conditions of the study area is essential for interpreting the spatial and temporal characteristics of wind resource distribution. Based on the data from the wind measurement towers (Mast 4#, Mast 5#, and Mast 6#), a comprehensive analysis is conducted on the monthly averages of air temperature, air pressure and relative humidity at the three observation towers (**Figure 4**). Air temperature at all three masts exhibits a consistent seasonal cycle, characterized by cold winters and hot summers. During the winter months (January, February and December), the air temperature is relatively low, ranging between −5 °C and −1 °C. In the summer months (June–August), the air temperature is relatively high, exceeding 20 °C, with the maximum monthly average reaching 26.14 °C (Mast 4#). Air pressure varies with the months, with higher values in winter and lower values in summer. For example, at Mast 4#, the air pressure from November to the following January ranges from 101.88 hPa to 102.33 hPa. In summer, air pressure is relatively low, which at certain towers ranges from 100.61 hPa to 100.88 hPa. Relative humidity shows an inverse seasonal trend compared with air pressure, i.e., it is generally higher in summer (exceeding 80% in some towers). In winter, relative humidity is low. For instance, the January average of the relative humidity at Mast 4# is 54.59%.

The variation trends of these meteorological elements are broadly consistent across the three observation towers, but there are certain differences in values, which may be related to factors such as the specific geographic locations of the observation towers.

3.1.2. Air Density

Wind energy potential is jointly affected by wind speed and air density. In offshore environments, where air humidity is relatively higher than over land, conventional methods for calculating air density may introduce relatively large errors. To address this, in this study, the control equations of dry air and water vapor are used jointly to calculate air density. The calculation results are shown in **Figure 5**, which presents the monthly air density of three observation towers (Mast 4#, Mast 5# and Mast 6#). The results indicate that the air density at the three observation towers shows similar seasonal variations, with higher values in winter (approximately 1.300–1.325 kg·m^{-3}) and lower values in summer (around 1.150–1.175 kg·m^{-3} during June–August). Although the general trends are similar, slight differences exist in air humidity values among the towers, and the values at Mast 4# are generally slightly higher than those at the other two towers. The curve of the monthly site averages reflects the overall monthly fluctuation trend, and the overall average in all months and at all sites remains at a relatively stable level of approximately 1.230 kg·m^{-3}, which can be used as a reference for the average air density.

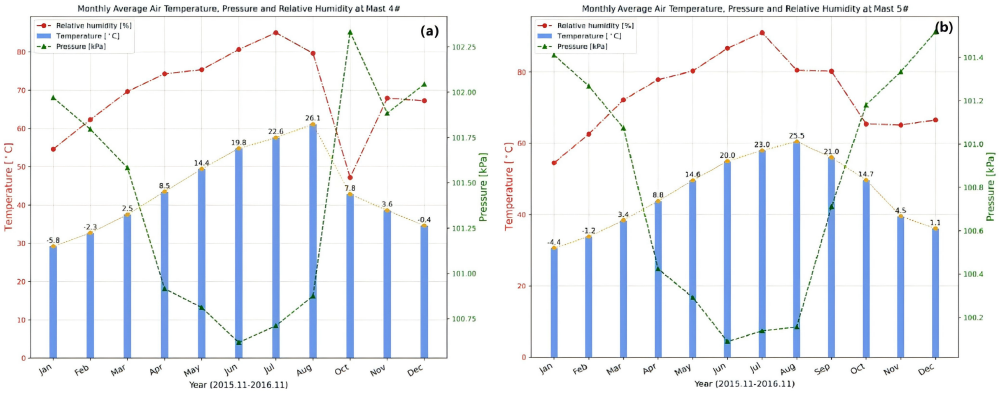

Figure 4. *Cont.*

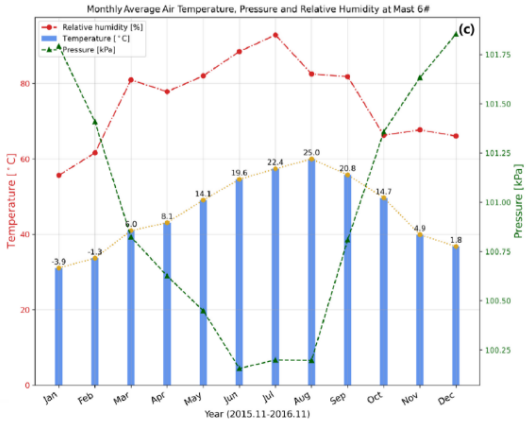

Figure 4. Monthly averages of temperature, air pressure, and relative humidity at (**a**) Mast 4#, (**b**) Mast 5#, and (**c**) Mast 6#.

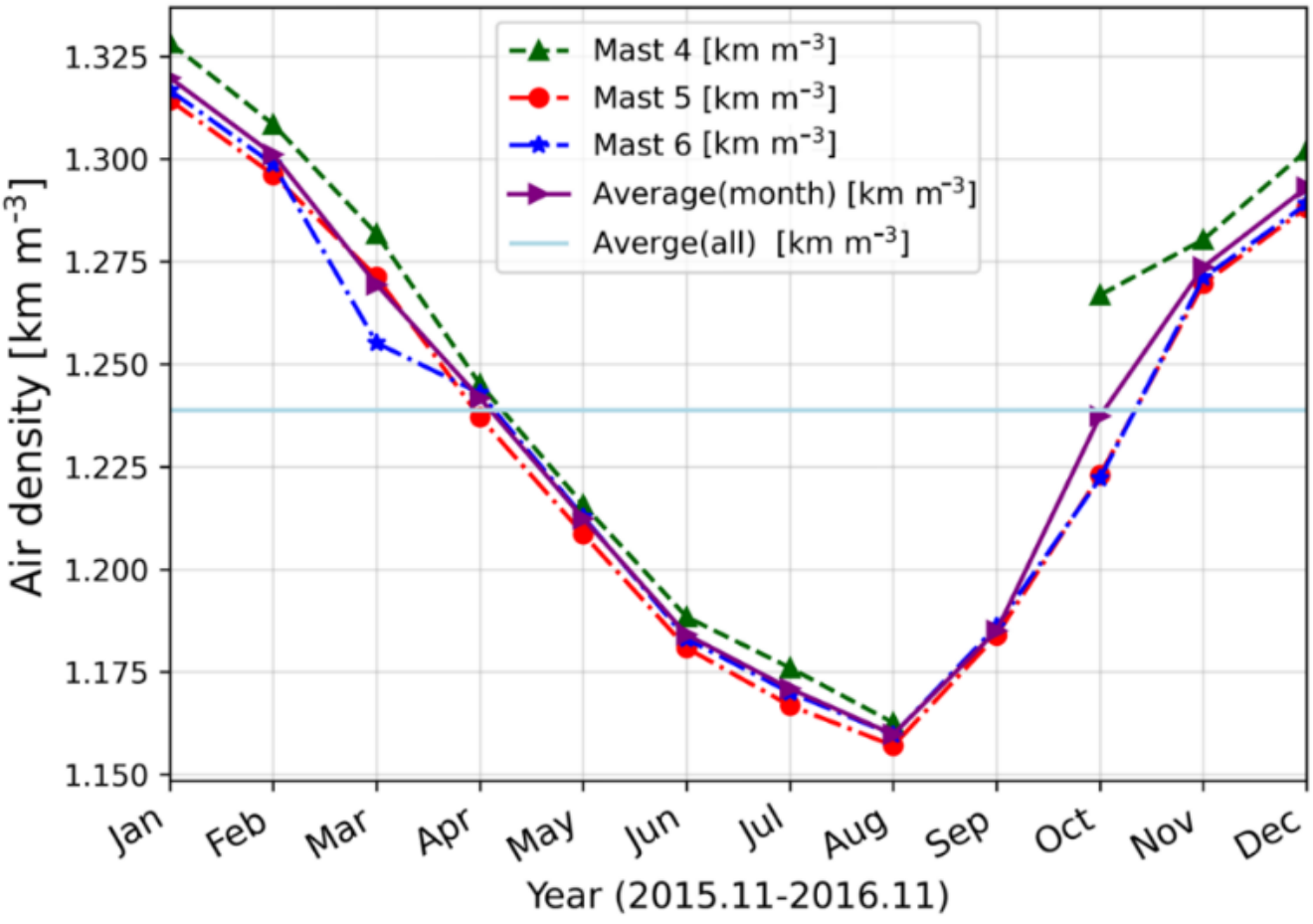

Figure 5. Monthly average air density at Mast 4#, Mast 5# and Mast 6#.

3.2. Assessment of SAR-Derived Wind Energy

3.2.1. Vertical Extrapolation of Wind Speed to Turbine Hub Height

The sea-surface wind speed retrieved based on satellite remote sensing data is only available at a height of 10 m. However, for wind energy applications, it is necessary to extrapolate retrieved results to the turbine hub height, typically around 100 m. Based on the method proposed by Nie and Li [50], this study performs vertical extrapolation of SAR-derived sea-surface wind speed to various heights. A monthly analysis of the overall wind energy situation in the Zhuanghe offshore area (122.5° E–124.0° E, 38.5° N–40.0° N) is conducted based on the SAR-retrieved wind field products during 2017–2022 (**Table 3**). The data for each month are fitted with a Weibull distribution, and the Weibull scale and shape parameters are estimated based on these monthly data. In addition, the above-mentioned two parameters are used to calculate the characteristic elements of wind energy. **Table 3** presents the average wind speed, the maximum wind speed, wind power density, and the Weibull scale and shape parameters at different heights of 10 m, 80 m and 100 m for each month.

3.2.2. Validation with Station Measurements

To verify the reliability of the vertical extrapolation, the extrapolated SAR wind speed is compared with the in-situ measurements from the wind measurement towers. **Figure 6** shows the comparison results of the monthly average wind speed between SAR-derived and the observation tower data at different heights. The results indicate that the deviations between these two data types at the heights of 10 m, 40 m, 80 m and 100 m are 0.07, 0.2, 0.15 and 0.22, respectively, and all are positive values (SAR-derived data minus measurements), i.e., the monthly average wind speed obtained from the SAR data is higher than that obtained from the observation towers. The root mean square errors between the SAR-derived and observed wind speed at the heights of 10 m, 40 m, 80 m and 100 m are 0.30, 0.37, 0.38 and 0.54, respectively. The largest deviation appears at a height of 100 m (0.54 $m \cdot s^{-1}$), and the root mean square errors at other heights are all less than 0.40 $m \cdot s^{-1}$. The correlation coefficients between these two data types at the heights of 10 m, 40 m, 80 m and 100 m are 0.96, 0.90, 0.85 and 0.73, respectively. The correlation is significant at the 0.05 level ($p < 0.05$) (**Table 4**). Moreover, the above three assessment indicators demonstrate a declining trend in indicating accuracy with increasing height, which is primarily attributed to the uncertainties introduced during the vertical extrapolation of wind speed.

3.2.3. Monthly Variations in the SAR-Derived Wind Speed and Wind Power Density

In this section, we examine the monthly variations in the SAR-derived wind speed and wind power density at different heights, as shown in **Figure 7**. The results indicate that the temporal variations in wind power density closely follow those of both the average and maximum wind speed across all four heights. Specifically, the three elements begin to rise in January, reach the first peak in February, then decrease to a minimum in June and July, and subsequently increase again, peaking in November. A slight decline is observed in December.

Furthermore, **Figure 8** displays the comparison of the monthly wind power density among different heights. It can be found that the monthly wind power density increases with height, consistent with the general increase in wind speed with altitude. Throughout the year, the wind power density is the lowest in June or July, exhibiting a left-right symmetrical distribution (double-peak pattern). Specifically, at 10 m height, the wind power density falls below 100 $W \cdot m^{-2}$ in June and July but remains above this value in the other months. At 40-m height, the wind power density drops below 150 $W \cdot m^{-2}$ in June and July, and it is higher than 150 $W \cdot m^{-2}$ in the other months. At heights of 80 m and 100 m, the wind power density is higher than 150 $W \cdot m^{-2}$.

Table 3. Average wind speed (V_{mean}), maximum wind speed (V_{max}), wind power density (WPD) and Weibull Parameters at different heights.

Month	Height (m)	V_{mean} (m·s^{-1})	V_{max} (m·s^{-1})	WPD (W·m^{-2})	Weibull Parameters	
					k	c (m·s^{-1})
Jan	10	6.30	9.15	267.99	2.40	7.10
	40	6.44	9.37	287.31	2.39	7.26
	80	6.52	9.48	298.35	2.39	7.36
	100	7.39	9.52	302.29	2.39	7.39
Feb	10	6.37	9.67	294.93	2.19	7.20
	40	6.63	10.05	331.25	2.19	7.48
	80	6.88	10.46	372.52	2.19	7.77
	100	6.97	10.59	386.64	2.19	7.87
Mar	10	5.39	8.52	186.77	2.03	6.08
	40	6.11	9.81	279.52	1.98	6.89
	80	6.32	10.18	311.22	1.97	7.13
	100	6.46	10.41	333.03	1.97	7.29
Apr	10	4.63	7.22	112.92	2.08	5.22
	40	5.53	8.78	198.58	2.01	6.24
	80	5.99	9.55	254.20	2.00	6.76
	100	6.95	9.82	276.24	2.01	6.95
May	10	4.74	6.93	105.95	2.37	5.35
	40	5.45	8.00	162.08	2.35	6.15
	80	5.85	8.59	200.57	2.35	6.60
	100	5.99	8.80	215.89	2.34	6.76
Jun	10	4.28	6.76	86.60	2.04	4.83
	40	4.84	7.69	126.78	2.01	5.46
	80	5.16	8.22	154.20	2.01	5.82
	100	5.26	8.36	162.93	2.01	5.93
Jul	10	4.31	6.79	87.52	2.05	4.87
	40	4.84	7.66	125.13	2.03	5.47
	80	5.13	8.12	149.03	2.03	5.79
	100	5.23	8.29	158.19	2.03	5.91
Aug	10	5.07	7.31	121.65	2.44	5.72
	40	6.19	7.49	154.93	2.42	6.19
	80	5.71	8.27	174.77	2.41	6.44
	100	5.78	8.38	181.77	2.41	6.52
Sept	10	5.61	8.30	176.33	2.30	6.33
	40	5.95	8.83	211.44	2.29	6.72
	80	6.13	9.11	231.67	2.29	6.92
	100	6.19	9.20	238.31	2.28	6.98
Oct	10	6.04	9.58	258.44	2.02	6.82
	40	6.34	10.10	300.48	2.00	7.15
	80	6.50	10.36	324.56	2.00	7.33
	100	6.53	10.45	331.78	1.99	7.37
Nov	10	6.90	9.80	327.08	2.52	7.78
	40	7.14	10.14	362.37	2.52	8.05
	80	7.26	10.31	380.90	2.52	8.18
	100	7.30	10.37	387.04	2.52	8.23
Dec	10	6.55	9.32	284.58	2.51	7.38
	40	6.78	9.66	316.31	2.50	7.64
	80	6.90	9.84	334.41	2.50	7.78
	100	6.94	9.90	340.41	2.50	7.83

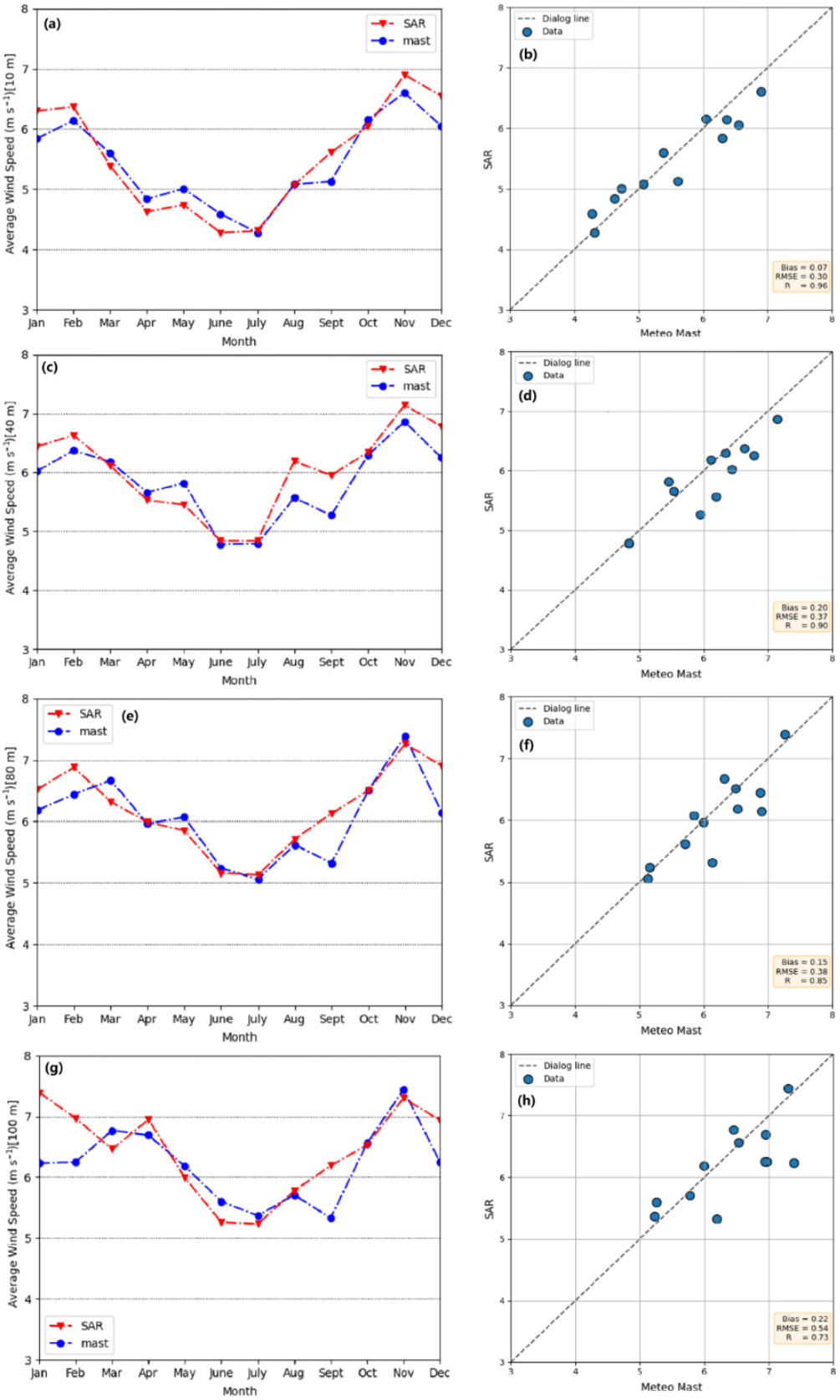

Figure 6. Comparison of the monthly average wind speed between the SAR-derived data (SAR) and the measurements (mast) at Mast 4# at heights of 10 m, 40 m, 80 m and 100 m.

Table 4. Statistical Parameters of SAR and Mast 4# Data at Different Heights

Statistical Parameters	Height (m)			
	100	**80**	**40**	**10**
Slope (m/s)	0.65	0.81	0.70	0.79
Intercept (m/s)	2.00	1.06	1.52	1.04
Bias (m/s)	0.22	0.15	0.20	0.07
RMSE (m/s)	0.54	0.38	0.37	0.30
Corr	0.73 ($p < 0.05$)	0.85 ($p < 0.05$)	0.90 ($p < 0.05$)	0.96 ($p < 0.05$)

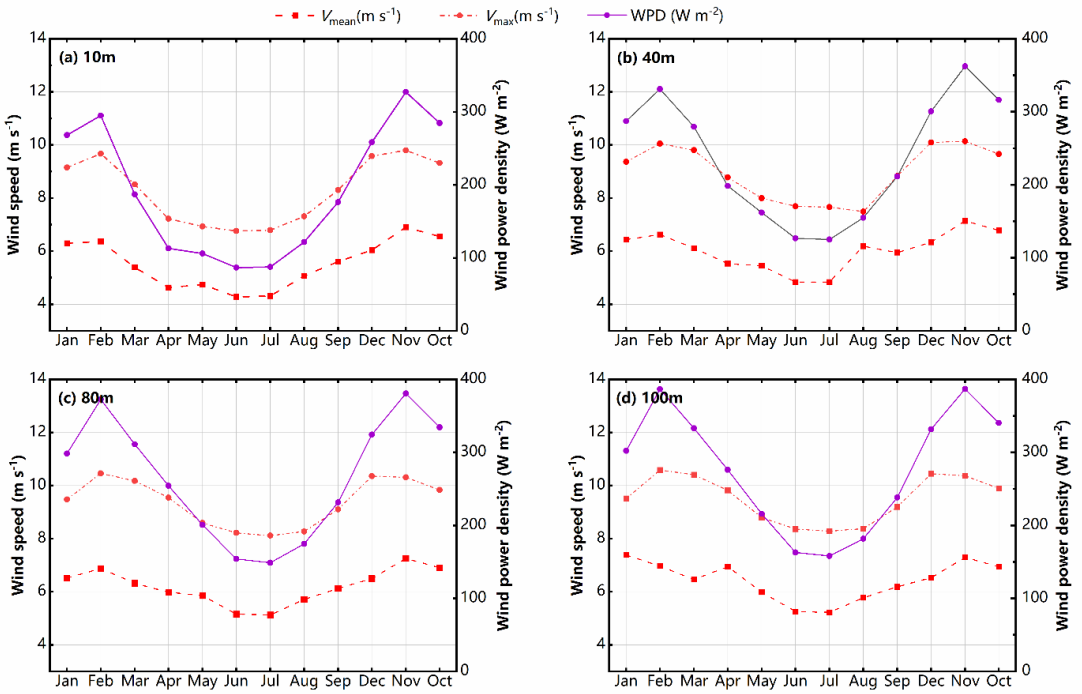

Figure 7. Monthly variations in wind speed and average wind power density at heights of (**a**)10 m, (**b**)40 m, (**c**) 80 m, and (**d**)100 m.

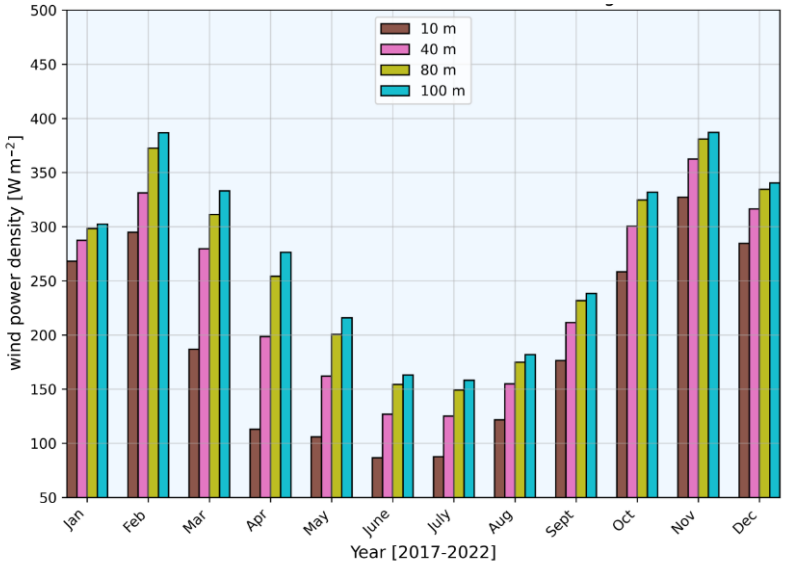

Figure 8. Comparison of the monthly wind power density among heights of 10 m, 40 m, 80 m and 100 m.

3.3. Analysis of Wind Energy Potential in the Zhuanghe Offshore Area

3.3.1. Frequency Distributions of Wind Speed and Wind Direction

To further analyze the seasonal differences in wind energy parameters (average wind speed, maximum wind speed and wind power density), the wind speed frequency distributions and the wind rose diagrams at a height of 100 m are provided for each season, as presented in **Figure 9**. The correlation coefficients of all Weibull fittings exceed 0.98 and the correlation is significant at the 0.01 level ($p < 0.01$). In terms of wind speed frequency distributions, the wind speed frequency shows a good fit with the Weibull distribution for each season, indicating statistical consistency in the wind regime. The wind rose diagrams reveal that the prevailing wind directions vary seasonally and follow a counterclockwise rotational pattern throughout the year.

In spring, the prevailing wind directions are relatively diverse in the Zhuanghe offshore area, mainly originating from the western sector. The overall average wind speed remains moderate. The prevailing wind directions with a proportion of more than 8% are westerly-southwesterly (WSW), southwesterly (SW), southerly-southwesterly (SSW) and southerly (S) wind. The wind directions with frequencies of 6%–8% are westerly (W), northwesterly (NW) and northerly-northwesterly (NNW) wind.

In summer, wind directions in the Zhuanghe offshore area become more concentrated compared with those in spring, and the average wind speed shows a slight increase. In terms of the prevailing wind directions, the frequencies of more than 11.4% appear in southerly (S) and southerly-southeasterly (SSE) wind. The wind directions with frequencies of 5.7%–8.6% are southeasterly (SE) and easterly-southeasterly (ESE).

In autumn, the prevailing wind directions remain concentrated, and the average wind speed is relatively larger. Notably, three prevailing wind directions exhibit average wind speed above 11 $m \cdot s^{-1}$: northerly (N, 13.9%), northerly-northwesterly (NNW, 12.8%) and northwesterly (NW, 10%).

Winter displays the most concentrated prevailing wind direction pattern, and the main prevailing wind directions are northerly-northwesterly (NNW) and northerly (N). Among them, the proportion of northerly-northwesterly wind is 19.6%, and the proportion of northerly wind is 15.2%. Both directions feature average wind speed exceeding 11 $m \cdot s^{-1}$.

3.3.2. Spatial Distribution of Wind Speed

The spatial distribution of wind resources is essential for the effective planning and layout of wind farms. Based on the spatial distribution maps of seasonal average wind speed at the heights of 10 m and 100 m (**Figure 10**), the following characteristics can be summarized.

The spatial distribution of the average wind speed at the 10 m and 100 m heights shows distinct seasonal characteristics. In spring, the 10 m average wind speed is relatively low, with a high-value area located in the central-northern region. At 100 m height, the average wind speed increases, and the high-value area expands. In summer, the 10 m average wind speed is more scattered, with slightly higher values in the central region. The 100 m average wind speed increases overall, and its central high-value area becomes more prominent. In autumn, the 10 m average wind speed increases markedly, with a high-value area in the southern region. At 100 m, the average wind speed further increases, and its high-value area becomes even wider. In winter, the 10 m wind speed is relatively high, with a prominent high-value area in the southern part. At 100 m, the average wind speed reaches its seasonal peak, and the high-value area expands further.

Overall, the wind speed distribution in the study area is remarkably affected by seasonal climatic conditions and geographical factors. Across all seasons, the average wind speed at the 100 m height is higher than that at the 10 m height, and spring and winter are peak seasons for wind energy. As height increases, the high-value range of wind speed tends to expand. The spatial distribution of average wind speed and the location and extent of high-value wind speed areas are characterized by pronounced seasonal variations, reflecting the dynamic and complex nature of the local wind field as modulated by seasonal atmospheric circulations.

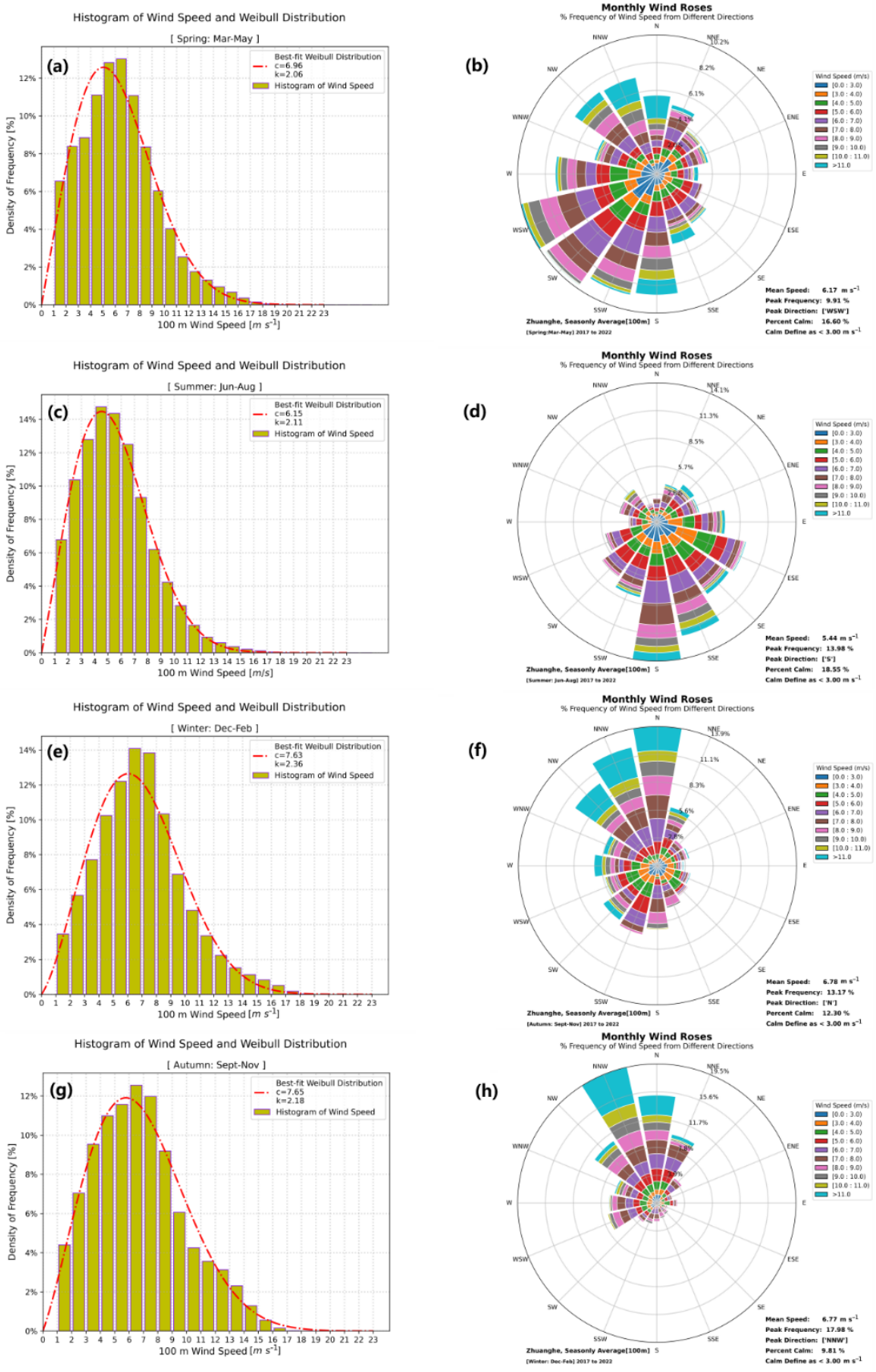

Figure 9. Wind speed frequency distributions and wind rose diagrams at a height of 100 m in different seasons.

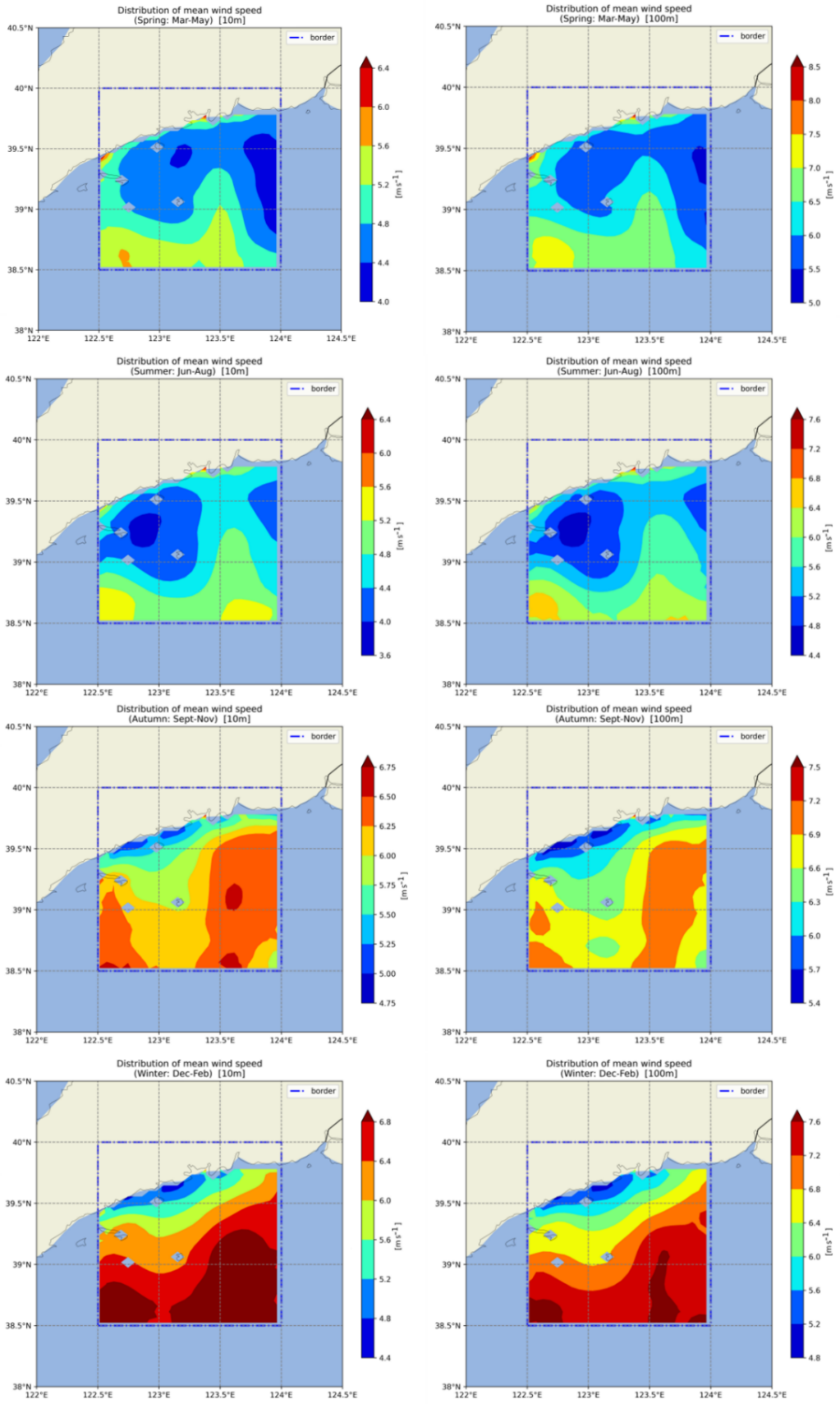

Figure 10. Spatial distribution of the average wind speed at the heights of 10 m and 100 m in different seasons.

4. Discussion

4.1. Comparison of the Satellite-Derived Wind Product with the ERA5 Reanalysis Data

Based on the ERA5 data, we conduct a large-scale analysis of the offshore wind power density in the Zhuanghe area. The ERA5 product is a global reanalysis dataset provided by the ECMWF, which features strong temporal continuity (updated hourly) and wide global coverage. In this research, 11 years of the ERA5 data from 2014 to 2024 are obtained for analyzing wind energy.

The analysis indicates that the wind speed in the Zhuanghe offshore area is stable. From the coast to the open sea, the wind speed gradually increases, with annual average values of 6–10 $m \cdot s^{-1}$. The wind speed is relatively higher in spring and winter and relatively lower in summer and autumn. According to statistics, the effective available hours (defined as hours with wind speed of 3–25 $m \cdot s^{-1}$) in 2021 are 7089 h, accounting for 80.92% of the whole year. The diurnal variation pattern shows that the wind speed tends to be higher during dawn and dusk. Specifically, the wind speed gradually decreases between 4:00 and 11:00 (local time), gradually increases until around 19:00 (local time), and then declines again. The wind speed conditions are suitable for the development and construction of wind farms. The high-frequency wind direction sectors at various heights are basically concentrated in the range from northerly-northwesterly (NNW) to easterly-northeasterly (ENE), with the prevailing wind direction being northerly-northeasterly (NNE, frequency of about 10%).

Using the ERA5 data, we calculate the wind power density at a resolution of 0.25° over the entire Zhuanghe offshore area. The results indicate that the wind power density gradually decreases from the open sea to the nearshore areas, mainly in the range of 200–300 $W \cdot m^{-2}$ (**Figure 11**).

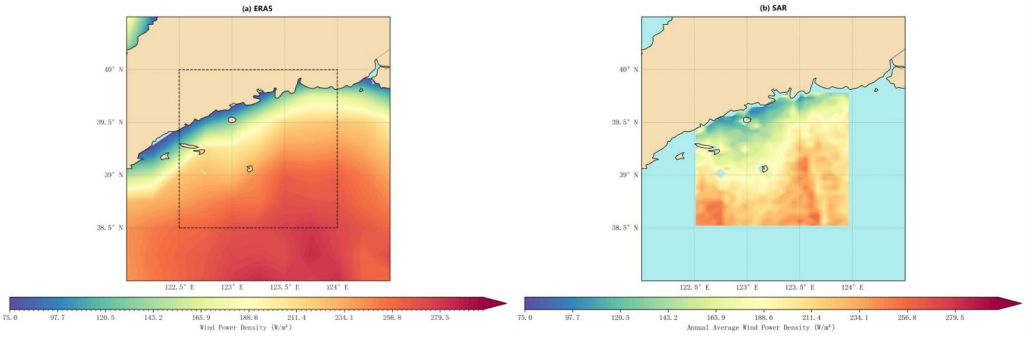

Figure 11. Wind power density maps from the (**a**) ERA5 data at the height of 10 m and (**b**) SAR-derived in the Zhuanghe offshore region.

Through the comparison, it is evident that the ERA5 product is suitable for the large-scale and long-term assessment of wind energy potential. Its advantages lie in excellent temporal continuity and extensive spatial coverage, enabling continuous and dynamic analyses of offshore wind speed and direction. However, due to its relatively low spatial resolution, the ERA5 wind data is limited in its ability to microscale variations in wind fields, particularly in coastal zones or regions with complex terrain. The wind power density from the SAR retrievals has a good correlation with that from the ERA wind data, which reflects that the SAR data are reliable for high-resolution evaluations of offshore wind resources.

ERA5 and SAR satellite data each offer distinct advantages in wind energy assessment (**Figure 12**). The ERA5 product is characterized by its global coverage, long time series and cost-efficiency, making it suitable for broad-scale wind energy planning. SAR satellite data, with high spatial resolutions and precision in local measurements, is particularly useful for detailed, site-specific evaluations. In practical applications, the complementary strengths of both dataset types can be leveraged. The ERA5 product

can serve as a baseline for large-scale planning, while SAR-derived data can be employed for refined site selection and validation, achieving a more comprehensive and accurate wind resource assessment.

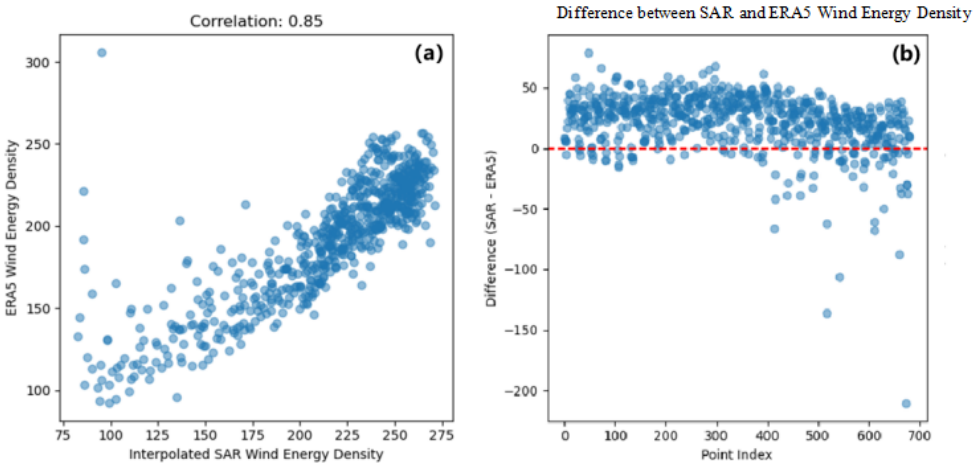

Figure 12. (**a**) Scatter distributions of the SAR-derived and ERA5 wind power densities and (**b**) the deviations distribution of the SAR-derived wind power density relative to the ERA5 data.

4.2. Quantifying the Effect of Sample Size on the Accuracy of SAR Wind Retrievals

The sample size of SAR images may have an impact on the accuracy of wind retrievals, and thus, we evaluate this influence using a method based on simulation data. Specifically, a pair of known Weibull parameters is selected, and the Weibull probability density function with these parameters is used to randomly generate a time series of wind speed. Subsequently, based on the simulated wind speed, we use the fitting method to fit and estimate the values of the Weibull parameters. The estimated Weibull parameters obtained through fitting are subsequently used to calculate wind power density, and the accuracy of the estimations is evaluated by comparing them with the known reference values. **Figure 13** shows the variation in errors with wind speed samples. Obviously, the estimation errors are inversely related to the sample size of wind speed. When there are 500 samples, the estimation error of the wind energy density falls within ±3%, demonstrating high reliability. In terms of engineering applications, jointly using long-term SAR satellite data, such as the data from Sentinel-1, EnviSat and RADARSAT satellites, it is possible to compile more than 20 years of historical data. Through this method, a higher accuracy wind energy product can be obtained, with sample sizes ranging from 1000 to 1500.

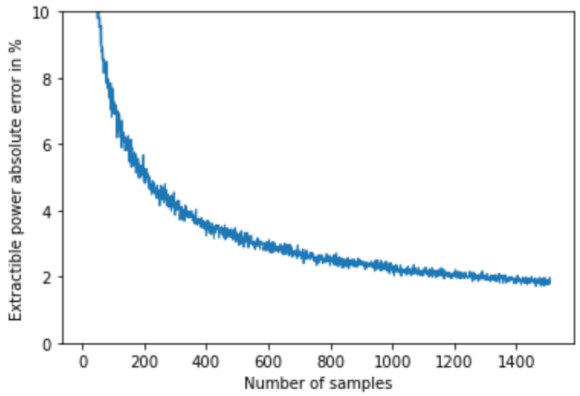

Figure 13. Correlation coefficient of wind power density between the SAR-derived and ERA5 data.

Notably, when the sample size reaches around 800–1000, the correlation coefficient between the SAR-derived and ERA5 wind power densities stabilizes. According to the Chinese meteorological industry standard, i.e., Technical guideline on investigation and assessment of offshore wind energy resource using remote sensing data (QX/T 584—2020), the sample number of SAR remote sensing images is not less than 400 scenes for wind energy assessment. Therefore, the SAR data of this study is sufficient to obtain real and reliable wind power density products.

4.3. Uncertainty Analysis

4.3.1. Uncertainties in SAR-Derived Sea Surface Wind Speed

The uncertainties in the sea surface wind speeds retrieved from SAR in this study are influenced by the coupling of multiple physical factors. Variations in monsoon activity, complex coastal topography, and the dynamic evolution of sea states directly affect the characteristics of SAR backscatter signals. Consequently, these factors lead to complex features in the spatial distribution and seasonal variability patterns of the retrieved wind speeds. Furthermore, in shallow and variable coastal environments, intricate land-sea interactions, water depth variations, and near-shore flow disturbances further increase the difficulty of SAR wind field retrieval, imposing distinct limitations on wind resource assessment in such scenarios. These uncertainties exert a non-negligible impact on the accuracy of retrieved sea surface wind speeds and the subsequent interpretation of wind resource distribution characteristics, necessitating explicit consideration in this study.

4.3.2. Critical Analysis on Vertical Extrapolation Uncertainty

This study specifically supplements a critical analysis of vertical extrapolation uncertainty, examining its potential impacts from both qualitative and quantitative perspectives. Qualitatively, models such as the logarithmic law and power law, relied on by vertical extrapolation, are all based on ideal atmospheric boundary layer assumptions. However, the spatiotemporal heterogeneity of atmospheric stability, sudden changes in near-sea surface roughness, and topographic disturbances in the actual observation area lead to deviations between model assumptions and the real environment, thereby introducing systematic uncertainty. Quantitatively, error propagation path analysis reveals that random errors (e.g., instrument noise, retrieval algorithm deviations) and systematic errors of SAR wind field retrieval values at 10 m height are amplified when transmitted to the 100 m hub height via vertical extrapolation formulas. Among them, random errors accumulate linearly or non-linearly, while systematic errors are further exacerbated by the sensitivity of model parameters. Ultimately, the relative error of wind speed estimation at 100 m height can reach 8%–15%, directly resulting in a significant widening of the confidence interval for wind energy density, a core parameter for wind farm planning, which reduces the reliability and accuracy of the confidence interval. This in turn exerts a cascading impact on the science of wind farm layout optimization, power generation prediction, and investment risk assessment, highlighting the indispensable role of vertical extrapolation uncertainty in offshore wind resource assessment and providing directions for subsequent error correction by optimizing extrapolation model parameters and integrating multi-source data.

5. Conclusions

In this study, SAR products from both domestic and international sources are utilized to assess wind energy resources in the Zhuanghe offshore area from 2017 to 2022, mainly including the Sentinel-1 satellite data from Europe and the GF-3 satellite data from China. Based on this dataset, we have completed the research on sea surface wind speed retrieval, data fusion of multi-source satellite remote sensing data, and vertical extrapolation technology for arbitrary heights, which is applied to wind resource assessment at specific sites. Comparison with the in-situ observation data from the meteorological wind measurement towers in the study area shows that the synthetic predicted wind speed has high consistency with the actual observation data (the RMSE of the monthly average data at the 100 m height is only 0.54 m s^{-1}, with a deviation rate of 5.53%). The findings of this

study demonstrate that SAR outperforms ERA5 in site-specific wind resource assessment in this region, based on its advantages in spatial resolution and local accuracy, which can better serve microscale offshore wind farm planning and design applications. Furthermore, the vertical extrapolation method enables wind parameter extrapolation at arbitrary heights and has shown good engineering applicability through testing (all correlation coefficients are ≥0.73 with $p < 0.05$). However, more in-situ measurement data are still needed for parameter calibration and optimization of this method to improve its technical performance.

Although the findings of this study have achieved certain innovations, there are still inherent uncertainties. For instance, the uncertainties in SAR-retrieved sea surface wind speed are influenced by the coupling of physical factors such as monsoon activity, complex coastal topography, and dynamic sea state evolution. The intricate interactions in shallow sea areas further increase the difficulty of wind speed retrieval. Additionally, the uncertainty in vertical extrapolation stems from deviations between the ideal assumptions of the model and the actual environment. After extrapolation, the errors at the 10 m height are amplified, leading to a relative error of 8%–15% in wind speed at the 100 m hub height. This significantly widens the confidence interval of wind power density, affecting the planning and assessment of offshore wind farms, and remains a research direction requiring improvement in the future. Therefore, future research will advance around four aspects: extending the observation period of wind measurement towers to address the temporal mismatch issue, and integrating machine learning algorithms to optimize the vertical extrapolation model for reducing uncertainties caused by sea state effects; extending the SAR-based wind resource assessment method to similar offshore areas with data scarcity and complex meteorological conditions in southern China (such as regions frequently hit by typhoons), and developing a universal technical scheme through multi-region validation; strengthening the coupling of SAR data with ERA5 and WRF numerical models, and leveraging the high spatial resolution advantage of SAR to improve the simulation accuracy of nearshore wind fields and enhance the accuracy of large-scale wind resource assessment; establishing a multi-dimensional uncertainty assessment framework covering factors such as SAR retrieval errors, extrapolation model errors, and the impact of sample size, and developing dynamic error correction tools.

Author Contributions

J.L. and F.Y. led the writing of this paper and acknowledge responsibility for the experimental data and results. L.Y. drafted the paper, and H.L., P.C., and X.R. led the consolidation of the dataset. This paper is written in cooperation with all of the co-authors. All authors have read and agreed to the published version of the manuscript.

Funding

This research was funded by "Research and Development of Intelligent Planning and Design Platform, and Research and Application Verification of Simulation Technology for Specific Scenarios Projects," grant number YJ25.004. The article publishing charge (APC) is funded by the Haizhuang Wind Power Co., Ltd., China State Shipbuilding Corp (CSSC).

Institutional Review Board Statement

Not applicable.

Informed Consent Statement

Not applicable.

Data Availability Statement

Data will be made available on request. This study primarily utilizes the datasets acquired from the GF-3 satellite datasets (https://satellite.nsmc.org.cn/PortalSite/Index.aspx), the C-SAR satellite datasets (https://drive.google.com/file/d/1SOEMud9oUq69gxbfcBkOvtUkZ3LWEpZJ/view?usp=sharing), the sentinel-1 Satellite datasets (https://dataspace.copernicus.eu/data-collections/sentinel-data/sentinel-1), ERA5

(https://cds.climate.copernicus.eu/datasets), GOOS (http://www.goosocean.org), NOAA (https://www.ndbc.noaa.gov), EMODnet (https://www.emodnet.eu), and Argo (http://www.argo.ucsd.edu).

Acknowledgments

The authors would like to thank GF-3 satellite datasets, C-SAR satellite datasets, sentinel-1 Satellite datasets, ERA5, GOOS, NOAA, EMODnet, and Argo for providing the data. We also thank the associate editor and two anonymous reviewers for their constructive suggestions and comments.

Conflicts of Interest

The authors declare that they have no known competing financial interests or personal relationships that could have appeared to influence the work reported in this paper. This paper reflects the views of the scientists and not the company.

AI Use Statement

The authors used DeepSeek-V3.2 solely for grammar checking, sentence structure refinement, and improving the readability of the English text in this manuscript. The authors take full responsibility for all academic content, including all ideas, data, analyses, and conclusions presented herein. The use of AI was thoroughly reviewed and supervised by the authors.

References

[1] International Energy Agency, 2020. World Energy Outlook 2020; IEA: Paris, France, 2020; pp. 1–25. Available online: https://www.iea.org/reports/world-energy-outlook-2020

[2] Hote, K.; Kaushik, R.; Tasnin, W. Global Offshore Wind Scenario: A Review. ECS Transactions 2022, 107(1), 11083–11103. [CrossRef]

[3] Barthelmie, R.J.; Pryor, S.C. Can satellite sampling of offshore wind speeds realistically represent wind speed distributions? Part II: Quantifying Uncertainties Associated with Distribution Fitting Methods. Journal of Applied Meteorology and Climatology 2003, 43, 739–750. [CrossRef]

[4] Elyouncha, A.; Eriksson, L.E.B.; Broström, G.; et al. Joint retrieval of ocean surface wind and current vectors from satellite SAR data using a Bayesian inversion method. Remote Sensing of Environment 2021, 260, 112455. [CrossRef]

[5] Yang, H.Y.; Fang, C.; Wang, S.; et al. On the ambiguity removal of wind direction derived from spaceborne SAR imagery using deep learning. Remote Sensing of Environment2024, 308, 114202. [CrossRef]

[6] Ricciardulli, L.; Wentz, F.J. A Scatterometry Geophysical Model Function for Climate-Quality Winds: QuikSCAT Ku-2011. Journal of Atmospheric and Oceanic Technology 2015, 32, 1829–1846. [CrossRef]

[7] Hersbach, H. CMOD5: An improved geophysical model function for ERS C-band scatterometry; European Centre for Medium Range Weather Forecasts (ECMWF): Reading, UK, 2003.

[8] Stoffelen, A.; Verspeek, J.A.; Vogelzang, J.; et al. The CMOD7 Geophysical Model Function for ASCAT and ERS Wind Retrievals. IEEE Journal of Selected Topics in Applied Earth Observations and Remote Sensing 2017, 10(5), 2123–2134. [CrossRef]

[9] Takeyama, Y.; Ohsawa, T.; Kozai, K.; et al. Comparison of geophysical model functions for SAR wind speed retrieval in Japanese coastal waters. Remote Sensing 2013, 5(4), 1956–1973. [CrossRef]

[10] Monaldo, F.; Jackson, C.; Li, X.; et al. Preliminary Evaluation of Sentinel-1A Wind Speed Retrievals. IEEE Journal of Selected Topics in Applied Earth Observations and Remote Sensing2016, 9(6), 2638–2642. [CrossRef]

[11] Lin, H.; Xu, Q.; Zheng, Q. An Overview on SAR measurements of sea surface wind. Progress in Natural Science 2008, 18(8), 913–919. [CrossRef]

[12] Zhang, B.; Lu, Y.; Perrie, W.; et al. Compact polarimetry synthetic aperture radar ocean wind retrieval: Model development and validation. Journal of Atmospheric and Oceanic Technology 2021, 38(4), 747–757. [CrossRef]

[13] Zhao, X.; Shao, W.; Hao, M.; et al. Novel Approach to Wind Retrieval from Sentinel-1 SAR in Tropical Cyclones. Canadian Journal of Remote Sensing 2023, 49(1), 2254839. [CrossRef]

[14] Gao, Y.; Zhang, J. Tropical Cyclone Wind Speed Retrieval from SAR Imagery Using A Neural Network. In Proceedings of the IEEE Radar Conference, Haikou, China, 15–19 December 2021; pp. 568–572. [CrossRef]

[15] Zanchetta, A.; Zecchetto, S. Wind direction retrieval from Sentinel-1 SAR images using ResNet. Remote Sensing of Environment 2021, 253, 112178. [CrossRef]

[16] Torres, R.; Snoeij, P.; Geudtner, D.; et al. GMES Sentinel-1 Mission. Remote Sensing of Environment

2012, 120, 9–24. [CrossRef]
[17] Majidi Nezhad, M.; Groppi, D.; Marzialetti, P.; et al. Wind energy potential analysis using Sentinel-1 satellite: A review and a case study on Mediterranean islands. Renewable and Sustainable Energy Reviews2019, 109, 499–513. [CrossRef]
[18] Chang, R.; Zhu, R.; Badger, M.; et al. Offshore wind resources assessment from multiple satellite data and WRF modeling over South China Sea. Remote Sensing 2015, 7(1), 467–487. [CrossRef]
[19] Fang, H.; Xie, T.; Perrie, W.; et al. Comparison of C-band quad-polarization synthetic aperture radar wind retrieval models. Remote Sensing 2018, 10(9), 1448. [CrossRef]
[20] Komarov, S.; Komarov, A.; Zabeline, V. Marine wind speed retrieval from RADARSAT-2 dual-polarization imagery. Canadian Journal of Remote Sensing 2012, 37(5), 520–528. [CrossRef]
[21] Kim, T.-S.; Park, K.-A.; Choi, W.-M.; et al. L-band SAR-derived Sea Surface Wind Retrieval off the East Coast of Korea and Error Characteristics. Korean Journal of Remote Sensing 2012, 28(5), 477–487. [CrossRef] (in Korean)
[22] Yao, R.; Shao, W.; Jiang, X.; et al. Wind speed retrieval from Chinese Gaofen-3 synthetic aperture radar using an analytical approach in the nearshore waters of China's seas. International Journal of Remote Sensing 2022, 43(8), 3028–3048. [CrossRef]
[23] Wan, Y.; Guo, S.; Li, L.; et al. Data quality evaluation of sentinel-1 and GF-3 SAR for wind field inversion. Remote Sensing 2021, 13(18), 3723. [CrossRef]
[24] Prajapati, J.; Chakraborty, A.; Shukla, B.P.; et al. Development of wind speed retrieval model using RISAT-1 SAR cross-polarized observations. Current Science 2020, 118(8), 1282–1286. [CrossRef]
[25] de Montera, L.; Remmers, T.; O'Connell, R.; et al. Validation of Sentinel-1 offshore winds and average wind power estimation around Ireland. Wind Energy Science 2020, 5(3), 1023–1036. [CrossRef]
[26] Ahsbahs, T.; Badger, M.; Karagali, I.; et al. Validation of sentinel-1A SAR coastal wind speeds against scanning LiDAR. Remote Sensing 2017, 9(6), 552. [CrossRef]
[27] Hadjipetrou, S.; Liodakis, S.; Sykioti, A.; et al. Evaluating the suitability of Sentinel-1 SAR data for offshore wind resource assessment around Cyprus. Renewable Energy 2022, 182, 1228–1239. [CrossRef]
[28] Rana, F.M.; Adamo, M.; Lucas, R.; et al. Sea surface wind retrieval in coastal areas by means of Sentinel-1 and numerical weather prediction model data. Remote Sensing of Environment 2019, 225, 379–391. [CrossRef]
[29] Miglietta, M.M.; Zecchetto, S.; De Biasio, F.; et al. A comparison of WRF model simulations with SAR wind data in two case studies of orographic lee waves over the Eastern Mediterranean Sea. Atmospheric Research 2013, 120–121, 127–146. [CrossRef]
[30] Salvação, N.; Bentamy, A.; Guedes Soares, C.; et al. Developing a new wind dataset by blending satellite data and WRF model wind predictions. Renewable Energy 2022, 198, 283–295. [CrossRef]
[31] Barone, M.; Galdi, C.; di Bisceglie, M.; et al. A Cross-Comparison Study on CYGNSS and Sentinel-1 wind Speed Products in Tropical Cyclones. In Proceedings of the 2024 IEEE International Geoscience and Remote Sensing Symposium, Athens, Greece, 7–12 July 2024; pp. 842–845. [CrossRef]
[32] Ahsbahs, T.; MacLaurin, G.; Draxl, C.; et al. US East Coast synthetic aperture radar wind atlas for offshore wind energy. Wind Energy Science 2020, 5(3), 1191–1210. [CrossRef]
[33] Badger, M. Satellite SAR Wind Resource Mapping in China (SAR-China); Technical University of Denmark, Risø National Laboratory for Sustainable Energy, Research Center Risoe: Kongens Lyngby, Denmark, 2009. Available online: https://backend.orbit.dtu.dk/ws/portalfiles/portal/3466486/ris-r-1706.pdf
[34] Chang, R.; Zhu, R.; Badger, M.; et al. Applicability of synthetic aperture radar wind retrievals on offshore wind resources assessment in Hangzhou Bay, China. Energies 2014, 7(5), 3339–3354. [CrossRef]
[35] Badger, M.; Fujita, A.; Orzel, K.; et al. Wind Retrieval from Constellations of Small SAR Satellites: Potential for Offshore Wind Resource Assessment. Energies 2023, 16(9), 3819. [CrossRef]
[36] Ma, Y.; Xu, J.; Wu, Y.; et al. Wind dataset assessment and energy estimation for potential future offshore wind farm development areas on the Scotian Shelf. Wind Energy Science 2025, 10, 2965–2999. [CrossRef]
[37] Palatos-Plexidas, A.; Gremmo, S.; van Beeck, J.; et al. Assessing the Accuracy of a Three-Year High-Resolution Mesoscale Wind Farm Wake Simulation with Lidar and Satellite Radar Data. Wind Energy Science Discuss. Preprints 2025. [CrossRef]
[38] de Montera, L.; Berger, H.; Husson, R.; et al. High-resolution offshore wind resource assessment at turbine hub height with Sentinel-1 synthetic aperture radar (SAR) data and machine learning. Wind Energy Science 2022, 7(4), 1441–1453. [CrossRef]
[39] Ahsbahs, T.; Badger, M.; Volker, P.; et al. Applications of satellite winds for the offshore wind farm site Anholt. Wind Energy Science 2018, 3(2), 573–588. [CrossRef]
[40] Owda, A.; Badger, M. Wind Speed Variation

Mapped Using SAR before and after Commissioning of Offshore Wind Farms. Remote Sensing 2022, 14(6), 1464. [CrossRef]

[41] Buonanno, S.; Cuozzo, G.; Fusco, A. Wind map retrieval from SAR data for offshore wind turbines positioning. In IEEE International Symposium on Industrial Electronics, Cambridge, UK, 30 June–2 July 2008; pp. 2311–2316. [CrossRef]

[42] Hasager, C.B.; Barthelmie, R.J.; Christiansen, M.B.; et al. Quantifying offshore wind resources from satellite wind maps: Study area the North Sea. Wind Energy 2006, 9(1–2), 63–74. [CrossRef]

[43] Hauser, D.; Abdalla, S.; Ardhuin, F.; et al. Satellite Remote Sensing of Surface Winds, Waves, and Currents: Where Are We Now? Surveys in Geophysics 2023, 44, 1357–1446. [CrossRef]

[44] Pierdicca, N.; Rocca, F.; Perissin, D.; et al. Numerical weather prediction models and SAR interferometry: Synergic use for meteorological and INSAR applications. In SAR Image Analysis, Modeling, and Techniques XI, Prague, Czech Republic, 21–22 September 2011; p. 817912. [CrossRef]

[45] Ivanova, T.; Porchetta, S.; Buckingham, S.; et al. Improving wind and power predictions via four-dimensional data assimilation in the WRF model: Case study of storms in February 2022 at Belgian offshore wind farms. Wind Energy Science 2025, 10(1), 245–268. [CrossRef]

[46] Khachatrian, E.; Asemann, P.; Zhou, L.; et al. Exploring the Potential of Sentinel-1 Ocean Wind Field Product for Near-Surface Offshore Wind Assessment in the Norwegian Arctic. Atmosphere 2024, 15(2), 146. [CrossRef]

[47] Liu, Q.; Babanin, A.V.; Zieger, S.; et al. Wind and Wave Climate in the Arctic Ocean as Observed by Altimeters. Journal of Climate 2016, 29, 7957–7975. [CrossRef]

[48] Doubrawa, P.; Barthelmie, R.J.; Pryor, S.C.; et al. Satellite Winds as a Tool for Offshore Wind Resource Assessment: The Great Lakes Wind Atlas. Remote Sensing of Environment 2015, 168, 349–359. [CrossRef]

[49] Zhou, Y.; Yang, B.; Yin, Q.; et al. Improved SAR Radiometric Cross-Calibration Method Based on Scene-Driven Incidence Angle Difference Correction and Weighted Regression. IEEE Transactions on Geoscience and Remote Sensing 2024, 62, 1–16. [CrossRef]

[50] Nie, B.; Li, J. Technical potential assessment of offshore wind energy over shallow continent shelf along China coast. Renewable Energy 2018, 128(Part A), 391–399. [CrossRef]